PORE-SCALE SIMULATION OF EXPERIMENTALLY REALIZABLE, OSCILLATORY FLOW IN POROUS ROCK

John F. Olson

Earth Resources Laboratory
Department of Earth, Atmospheric, and Planetary Sciences
Massachusetts Institute of Technology
Cambridge, MA 02139

ABSTRACT

We report new simulations of oscillating flow in porous rock. Our goal is to better understand the frequency dependence of pore-scale fluid motion, which should ultimately help us to interpret attenuation and electroseismic measurements.

We use a lattice gas cellular automaton (Rothman and Zaleski, 1997) to perform the calculations in a pore space geometry measured from Fontainebleau sandstone by X-ray microtomography (Spanne et al., 1994; Auzerais et al., 1996). We chose this method because it is fast and efficient in the complex geometry of the porous rock. We show that the Biot critical frequency (Biot, 1956) is accessible to simulation, and we perform simulations at a range of frequencies around the critical frequency. In addition, we show that the dynamical properties of the lattice gas fluid can be mapped onto reasonable real fluids.

As the frequency varies through the critical range, we observe qualitative and quantitative changes in the amplitude and phase of fluid velocity distributions. We also report preliminary calculations of the local viscous dissipation, which should provide a means to compare our simulations with existing theories of attenuation (e.g., Johnston et al., 1979; Dvorkin and Nur, 1993; Akbar et al., 1994).

INTRODUCTION

Geophysical exploration relies on remote sensing techniques to reveal the structure of the rock below the surface. Often our goal is to predict the location of some subsurface fluid of economic importance, either oil, water, or natural gas that we wish to extract as efficiently as possible, or possibly carbon dioxide or some other waste product that can

be sequestered safely. Unfortunately, seismic measurements are not usually diagnostic for fluids. We can sometimes detect pockets of gas, but identifying which layers actually contain oil or brine, for instance, is beyond our technology.

Electroseismic measurements offer a potential means to detect actual flow in the subsurface. Seismic attenuation measurements may offer a means to detect the presence of fluids by observing the extra dissipation of acoustic energy due to viscous flow. In both cases, we can think of the pore-scale fluid motion as a transducer, coupling an input energy to an output energy. In the case of electroseismic measurements, electrical and acoustic energy are interconverted by the moving fluid. In the case of acoustic dissipation, some of the acoustic energy is transformed into heat by the fluid motion. In order to extract as much information as possible from the remotely sensed signal, we need to know as much as possible about how that transduction takes place. This knowledge is one of the reasons we study frequency dependence of pore-scale fluid motion in rock.

In addition, there have been experiments in which acoustic signals enhance the permeability of fluid bearing rock. Whatever mechanism is at work in these experiments, understanding it will involve examining the motion of fluids at the scale of a few pores in the rock. For remote sensing needs, to understand these laboratory experiments and to suggest new kinds of experiments, we need to know more about how fluids move at the scale of pores in the rock.

Laboratory measurements are irreplaceable, but measurement is limited because rock is opaque. There are few techniques which can observe the motion of fluid in the pores of a rock beyond a depth of a few microns. An exception is magnetic resonance imaging (MRI) (Guilfoyle et al., 1992; Tessier and Packer, 1998), which promises to be a highly valuable technique; at the present time, however, its resolution is coarse. Also, experiments are limited by the fact that the rock is chemically active. As we move fluids through the rock, we necessarily change the species adsorbed on the pore walls, which can have a significant effect on transport properties. We turn, therefore, to simulation because it allows us to observe the flow in great detail under a range of conditions, and because we can be assured of perfect reproducibility.

Method

The present work is not about reservoir scale simulation, but about simulation at a much smaller scale. Reservoir simulation has proved to be a valuable part of engineering practice, but the present work is concerned with simulating fluid motion at the scale of a few pores in the rock, that is, at a scale of a few tens of microns. At this scale, the geometry of the rock is complicated and applying sensible boundary conditions at all the surfaces of the pores becomes the hardest part of the calculation. We use, therefore, a lattice gas cellular automaton (Rothman and Zaleski, 1997) to compute the flow in these simulations because this method manages the boundary conditions in a particularly convenient way. It is also computationally efficient, highly parallelizable, and compact in memory so that we can look at large volumes of rock. In addition,

the lattice gas can be generalized to two phases, though the simulations in this paper will have a single liquid phase. We have considerable confidence in using this method, because it has been demonstrated to be valid by both theoretical measures (Appert *et al.*, 1995; Olson and Rothman, 1997) and by comparison with laboratory measurements of permeability (Auzerais *et al.*, 96).

To do simulation on the pore scale, we need to know the geometry of the rock at a resolution high enough to see individual pores, which is difficult. People have digitized thin sections and used them to obtain statistical properties, and then generated synthetic geometries with the same statistical properties (e.g., Lindquist *et al.*, 1996), but it is unclear what statistical properties one needs to measure and even whether they could be measured from a thin section. We use instead a rock geometry measured in three dimensions by X-ray microtomography (Spanne *et al.*, 1994) with a resolution of 7.5μm, which is fine enough to resolve much of the pore structure but still much too coarse to compute electroseismic results directly. We have begun to work on obtaining rock geometry at high resolution through MRI measurements; in addition, MRI may give us the means to test our simulations directly against measurement. So far, the resolution remains coarse.

Figure 1 shows a simple, three-dimensional rendering of a portion of the tomographically measured rock geometry. This is the pore space in which the simulations below were carried out. It has a volume of 600μm($80 \times 7.5\mu$m) on a side; we marked each of the 53,000 locations that are at the interface between rock and void with small, brown dots. We also marked the front edges of the simulation volume with a fine, gray line to guide the eye. In Figures 1a–c, we superimpose slices through the rock at different depths to show the complexity of the pore space. In Figure 1d, we show the rock alone in the orientation that will be used for all the other figures in the paper.

In our simulations, the rock geometry is present solely as a constraint on the fluid motion; the rock is absolutely rigid. In the real world, the rock is an elastic medium which responds to the same acoustic wave as the fluid and attenuates the signal separate from the fluid. The fluid motion is thus determined not only by the external pressure field, but by the motion of the rock as well. We hope to simulate this coupled physics at some point, but for the moment we will neglect the rock motion and compute only the motion of the fluid due to an externally imposed, oscillating pressure field.

Accessible Dynamical Regime

In the lattice gas method, we fill the pore space with a large number of particles that interact with each other only in collisions, which conserves mass and momentum. Fluid dynamics emerges as the average behavior of the particles, just as fluid dynamics is the average behavior of the molecules which compose a real fluid. As a consequence, we do not have complete freedom to choose such macroscopic fluid properties as speed of sound or viscosity. However, we have freedom to choose a time and a length scale, corresponding to the time between collisions and the distance between collision sites. For the present case, we identify the distance between collisions with the resolution of

the geometry data, 7.5μm, and we choose the time scale so that the speed of sound in the fluid is a physically reasonable 1500ms^{-1}. Then, the kinematic viscosity turns out to be high (4.3×10^{-4}m^{2}s^{-1}, or 430 times that of water) but within the range of viscosities observed in heavy oil. If we wished to simulate a fluid with the viscosity of water and the same speed of sound, we would need a spatial resolution 100 times higher and a time scale a thousand times smaller, which would make our calculations a billion times more demanding than the ones carried out so far. It is not unreasonable to suppose that such calculations could be carried out with more advanced computing facilities.

Given these dynamical parameters, what kinds of physics can we hope to observe? It turns out that the Biot critical frequency (Biot, 1956) is easily accessible to our simulations, so we can observe a variety of phenomena. Given a channel of diameter d filled with a fluid with kinematic viscosity η, the Biot critical frequency is $f_c = \frac{\pi \eta}{4 d^2}$. This is the frequency below which flow in the channel is expected to resemble Poiseuille flow. In the convoluted pore geometry of a rock, it is difficult to pick out any kind of "typical" diameter, but we can pick out a range that seems interesting. In the present case, pores range from 15 to 75μm, so we expect to see the dynamics in the medium change as the frequency varies from 60kHz to 1.5MHz. This range of frequencies is readily accessible in the simulation.

Simulations

We perform all our simulations in the same 600μm sample of pore space. The pore space is surrounded with an impermeable wall, and a buffer is created at each end of the rock. To drive fluid motion in the rock, we remove particles of fluid from the buffer on one end of the rock and replace them at the other end. This creates a pressure gradient and, consequently, fluid motion through the rock. The rate at which we move particles from one buffer to the other varies sinusoidally with time. In this way, we can create a pressure gradient which varies sinusoidally in time at a range of frequencies.

To obtain meaningful fluid dynamics, we need to average particle momenta and populations over many time steps. However, if we did that naively with sinusoidal forcing, we would expect to see no net motion. Instead, the appropriate way to average the flow is through its Fourier transform. At each node, we define the Fourier transform of density,

$$\mathcal{F}_\rho(\vec{x}, \omega) = \sum_t e^{i\omega t} \rho(\vec{x}, t) \tag{1}$$

and similarly for each component of momentum. Thus, at each time step we measure the density and momentum at each node, and sum them into their Fourier components as shown. We do not, in fact, calculate full Fourier transforms at every location, because that would require too much memory; we have observed that there is little energy at frequencies other than the driving frequency. Instead, we simply calculated the Fourier components at the driving frequency. (We also computed the components at half and

6–4

double the driving frequency, but as mentioned the energy at these frequencies was negligible.) After half a million time steps (25 to 2500 periods, depending on the frequency), we compute the average phase and amplitude at each location and write these data to a file. In what follows, we will see plots of the data and of the viscous dissipation, which can be computed from the data.

Computing Viscous Dissipation

To compute the viscous dissipation, we make use of a formula from Lamb (article 329) (Lamb, 1945):

$$
\Phi = \mu \left\{ 2 \left(\frac{\partial u}{\partial x} \right)^2 + 2 \left(\frac{\partial v}{\partial y} \right)^2 + 2 \left(\frac{\partial w}{\partial z} \right)^2 + \right.
$$
$$
\left. \left(\frac{\partial w}{\partial y} + \frac{\partial v}{\partial z} \right)^2 + \left(\frac{\partial u}{\partial z} + \frac{\partial w}{\partial x} \right)^2 + \left(\frac{\partial v}{\partial x} + \frac{\partial u}{\partial y} \right)^2 \right\}. \tag{2}
$$

Since our simulation results are Fourier components of the velocity field, we cannot apply this formula directly. We find that there is practically no energy at frequencies different from the driving frequency, so we will approximate the flow by a simple sinusoid at each location, i.e., $u_\alpha(\vec{x}) = A_\alpha(\vec{x})cos(\omega t + \delta_\alpha(\vec{x}))$ with ω the driving frequency, α the index of the Cartesian components of the velocity, and A_α and δ_α the amplitude and phase of the velocity component at each location in space. With this velocity field, then, the viscous dissipation integrated over one period of the driving is

$$
\bar{\Phi} = \frac{\mu \pi}{\omega} \left\{ 2 \sum_\alpha \left[\left(\frac{\partial A_\alpha}{\partial x_\alpha} \right)^2 + \left(A_\alpha \frac{\partial \delta_\alpha}{\partial x_\alpha} \right)^2 \right] + \right.
$$
$$
\left. \sum_{\alpha \neq \beta} \left[\left(\frac{\partial A_\alpha}{\partial x_\beta} + \frac{\partial A_\beta}{\partial x_\alpha} \right)^2 + \left(A_\alpha \frac{\partial \delta_\alpha}{\partial x_\beta} + A_\beta \frac{\partial \delta_\beta}{\partial x_\alpha} \right)^2 \right] \right\}. \tag{3}
$$

This formula requires 18 distinct derivatives of the velocity field, which makes it difficult to apply to the simulation data. The lattice gas method generates a velocity field which is necessarily noisy and which is defined only on a grid in space. Consequently, the derivatives must be replaced with finite differences, and the relative error due to the noise gets larger when we take these differences. In order to compute the approximate local viscous dissipation, then, we take considerable care with the simulations. In each case, data was accumulated over half a million time steps after an initial 50,000 time steps to let transient behavior decay. Such long simulations were needed to achieve low enough noise levels. To further reduce the noise before computing differences, we smoothed the velocity field by averaging over cubes of side length 3. (To be precise, at each fluid node, i.e., each lattice node which was not designated solid, we replaced the velocity with the mean value over all those fluid nodes within the cube of size 3 centered at the node. If some of those nodes were solid, they were omitted from the mean.) Finally, when we report our results, we coarse grain all the quantities—density,

Frequency (kHz)	Phase	Max. Speed (m/s)	Location
14	$\pi/6$	222	Main
28	$\pi/4$	180	Main
56	$\pi/3$	134	Main
141	$\pi/2$	70	Main
282	$17\pi/24$	34	Main
565	$\pi/3$	19	Secondary
1410	$\pi/3$	11	Buffer

Table 1: Velocity field properties as a function of driving frequency. The "Phase" is how far the maximum velocity lags behind the maximum driving flux. Biot critical phenomena are expected in the range 60kHz to 1.5MHz.

velocity, and dissipation rate—onto a grid three times larger than the simulation grid before reporting our results. By these means, we arrive at results which should be representative of real systems.

OBSERVATIONS

All of the simulations in this paper were performed in the same sample of pore space, shown in Figure 1. We omitted the forcing buffers, which are at the far left and right faces. Where we look tangent to an internal boundary in the rock, the dots line up, and we see a denser pattern. With a little imagination, one can begin to pick out some of the structure of the rock, but in the end a two-dimensional picture can only give a flavor of the structure. This particular view was chosen because there are two important channels through the rock which are closer to this face; these channels will become more apparent later on. Each subsequent image will have some fluid data superimposed upon the pore structure shown in Figure 1. In each case, the pressure gradient is applied along the x axis, which is from left to right.

Velocity Components

In these simulations, the flux of fluid was controlled, so fluid velocity is the quantity most directly related to the driving. For this reason, we begin by examining the flow field in the rock. At each driving frequency, we find the location where the velocity has the largest amplitude, and we show the vector field at the time during the oscillation when the velocity takes its largest value. Table 1 and Figure 2 summarize results from all the simulations.

In Table 1, we record the frequency of the driving in each simulation, the maximum speed of the fluid in the simulation, the phase lag between the maximum of the driving and this maximum velocity, and the location where the maximum velocity is attained. As a general observation, the velocities are large; so, too, are the dissipation rates and pressures, shown below. However, all the observed values are well within the range of

validity of the simulation method. While a real fluid would flow turbulently at such high speeds, this lattice gas model computes Stokes flow, so the results are valid for more physically reasonable laminar flow. The simulations were performed at such extreme conditions in order to be able to observe significant fluid dynamical phenomena above the statistical noise of the model. We could have forced the simulation more gently, and then the velocities and pressures would have been correspondingly smaller—and correspondingly harder to observe, requiring longer averaging.

At low frequencies, the velocity is nearly in phase with the driving, but as the frequency increases, the maximum velocity lags further behind the driving. Meanwhile, the maximum velocity also decreases with increasing frequency. Most interesting is that the location of the most rapid flow changes. At low frequencies, the velocity field is clearly dominated by a single channel, as we see in Figures 2a and 2b. When the frequency gets above 500kHz (Figure 2c), flow in a narrower, lower channel becomes more important than flow in the larger, upper channel. At the highest frequency, there is no longer any significant flow through the pore space, just oscillation at the forcing buffers, as shown in Figure 2d.

This is broadly the behavior that is expected. At low frequencies, the flow should be dominated by the largest channels available, but as the frequency increases, the largest channels will be the first to be dominated by inertial forces, stopping the macroscopic flow. Smaller channels never carry as much flux, but they remain active at higher frequencies. Just so, the main channel is significantly broader than the secondary channel, so it carries more flux at lower frequencies, but cuts off at higher frequencies, allowing the secondary channel to become more prominent.

Dissipation

From the velocity fields shown above, we can compute the local rate of viscous dissipation using Eq. (3). We summarize the results in Table 2 and Figure 3. It is curious that while the total dissipation rate declines with increasing frequency, the maximum dissipation has an anomalous minimum at 282kHz. In Figure 3, we plot a dot at each location in the pore space; the area and darkness of the dot correspond to the local viscous dissipation, normalized to the maximum dissipation in each case. We see that the dissipation field is strongly localized, even more so than the velocity field. In almost every case, nearly all the dissipation takes place in the main channel through which the flow is most rapid. The dissipation is still localized in the main channel even when the maximum velocity has shifted to the secondary channel at frequency 565kHz, as shown in Figure 3c, but the dissipation maximum moves to that channel at 1.4MHz in Figure 3d.

Figure 3a reveals another challenge in computing a meaningful viscous dissipation from the simulation. We see that there is strong dissipation at the edge of the simulation volume where the fluid enters the rock from the forcing buffers. This edge effect can hardly be considered indicative of the flow in the rock, yet it may be difficult to disentangle properly from the "real" dissipation. Perhaps a different forcing method, or

Olson

Frequency (kHz)	Max. Dissipation (mW)	Location	Total Diss. (W)
14	40	Main	43
28	18	Main	26
56	11	Main	15
141	5.3	Main	5.3
282	0.98	Main	2.6
565	2.8	Main	2.0
1410	0.33	Secondary	0.71

Table 2: Viscous dissipation as a function of driving frequency. The dissipation is strongly localised, and the maximum dissipation does not necessarily coincide with the maximum velocity.

performing the simulation in a periodic medium, would eliminate this problem. However, for the present paper we can make our qualitative observations without difficulty.

Pressure

The pressure fields are less illuminating than one might imagine because the velocity fields and the pressure fields are essentially complementary, where one is large, the other is small. We show four examples below (Figure 4), where we plot the amplitude of the pressure variation by the size of dots, and the phase of that variation (measured with respect to the phase of the forcing) by the color of the dots. Locations that are nearly in phase with the forcing are light grey and locations that are nearly opposite in phase, are black. Locations that are between these extremes are colored blue if their maximum precedes the maximum of the forcing, and green if their maximum follows after the maximum forcing. Because the pressure differences are largest where the flow is least, and vice versa, we see features in the pressure field which were not apparent in the velocity or dissipation fields. For example, in Figure 4a, at a low frequency where most of the flow takes place in the main channel, the secondary channel is clearly visible, whereas this channel is nearly invisible at a higher frequency (Figure 4c) where the flow in the secondary channel is large. The pressure field changes in phase with increasing frequency as did the velocity field. More interesting is the transition between pressure-driven viscous flow at low frequencies, indicated by large pressure amplitudes, to inertial flow at high frequencies where pressure variations (and velocities) remain small everywhere. Comparing the four cases plotted in Figure 4, note how the typical pressure amplitude changes from large at low frequency to small at high frequency.

CONCLUSIONS

We have shown that it is possible to predict flow in porous rock in response to an oscillating pressure field, and that the results of these simulations are qualitatively consistent with theoretical expectations. To make detailed comparisons with theory will require more extensive simulation on media which can be more simply characterized. More detailed comparison with experiments will have to await new techniques for measuring flow properties in three dimensions. However, it is clear that regimes of physical interest are accessible to simulation and that simulation yields information about flow fields which is not otherwise available. It is our hope that careful examination of the flow properties revealed by simulation will help us to better understand the effect of fluid saturation on seismic waves, and thus to provide a means to sense and characterize fluids remotely.

ACKNOWLEDGMENTS

REFERENCES

Akbar, N., G.Mavko, A. Nur, and J. Cvorkin, Seismic signatures of reservoir transport properties and pore fluid distribution, *Geophysics, 59*, 1222–1236, 1994.

Appert, C., J.F. Olson, D.H. Rothman, and S. Zaleski, Spinodal decomposition in a three-dimensional, two-phase, hydrodynamic lattice gas, *J. Stat. Phys., 81*, 181–197, 1995.

Auzerais, F.M., J. Dunsmuir, B.B. Ferréol, N. Martys, J. Olson, T.S. Ramakrishnan, and L.M. Schwartz, Transport in sandstone: A study based on three dimensional microtomography, *Geophysical Research Letters, 25*, 705–708, 1996.

Biot, M.A., Theory of propagation of elastic waves in a fluid-saturated porous solid. I. Low-frequency range, *J. Acoustical Society of America, 28*, 168–178, 1956.

Dvorkin, J. and A. Nur, Dynamic poroelasticity: A unified model with the squirt and the Biot mechanisms, *Geophysics, 58*, 524–533, 1993.

Guilfoyle, D.N., P. Mansfield, and K.J. Packer, Fluid flow measurement in porous media by echo-planar imaging, *J. Magnetic Resonance, 97*, 342–358, 1992.

Johnston, D.H., M.N. Toksöz, and A. Timur, Attenuation of seismic waves in dry and saturated rocks: II. Mechanisms, *Geophysics, 44*, 691–711, 1979.

Lamb, Sir Horace, *Hydrodynamics*, Dover Pub., 6th edition, 1945.

Lindquist, W.B., S.-M. Lee, D.A. Coker, K.W. Jones, and P. Spanne, Medial axis analysis of void structure in three-dimensional tomographic images of porous media, *J. Geophysical Research, 101*, 8297–8310, 1996.

Olson, J.F. and D.H. Rothman, Two-fluid flow in sedimentary rock: Simulation, transport and complexity, *J. Fluid Mechanics, 341*, 343–370, 1997.

Rothman, D.H. and S. Zaleski, *Lattice-Gas Automata: Simple Models of Complex Hydrodynamics*, Cambridge University Press, Cambridge, 1997.

Spanne, P., J.F. Thovert, C.J. Jacquin, W.B. Lindquist, K.W. Jones, and P.M. Adler, Synchrotron computed microtomography of porous media: Topology and transports, *Physical Review Letters, 73*, 2001–2004, 1994.

Tessier, J.J. and K.J. Packer, The characterization of multiphase fluid transport in a porous solid by pulsed gradient stimulated echo nuclear magnetic resonance, *Physics of Fluids, 10*, 75–85, 1998.
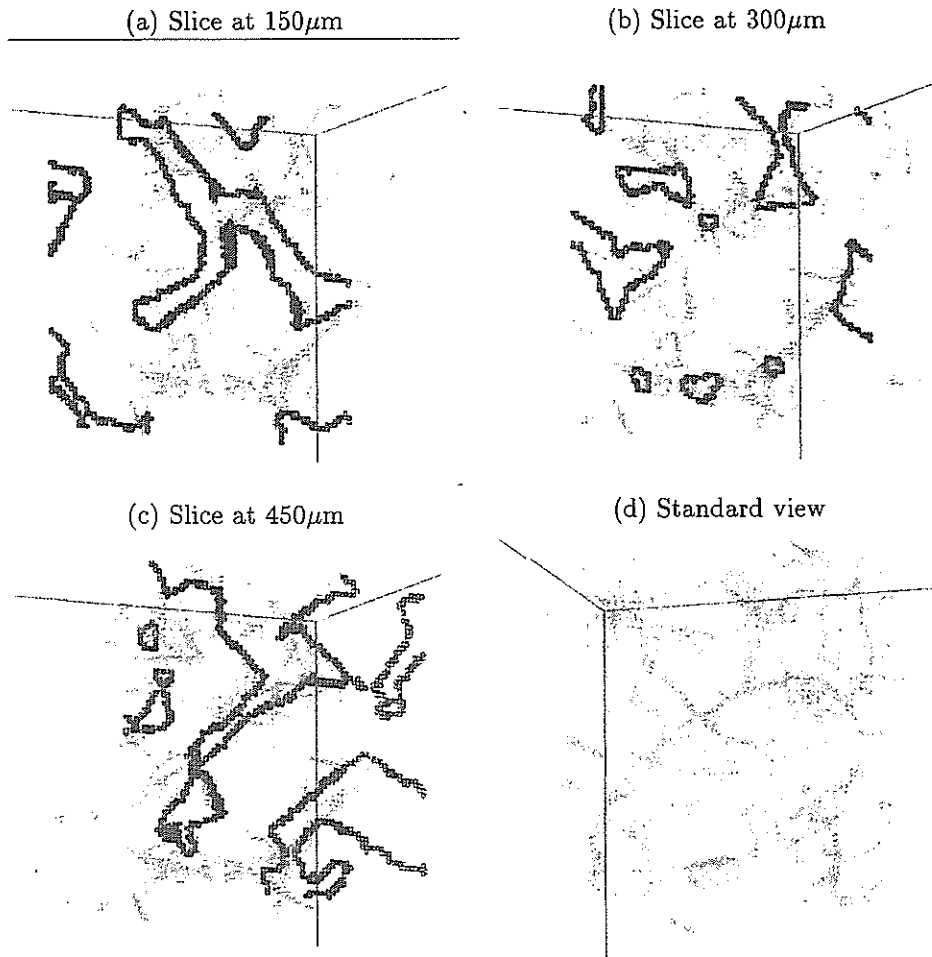
Oscillatory Flow in Porous Rock

(a) Slice at 150μm   (b) Slice at 300μm

(c) Slice at 450μm   (d) Standard view

Figure 1: Views of the simulation pore space. The rock was imaged by X-ray microtomography, which resolves the rock into cubes of size 7.5μm. Here we show the 600μm sample in which the simulations were computed. Each brown dot represents a cube which is at the interface between solid and void. In the simulations to follow, the forcing is applied along the x axis, which is into the page in the first three images, and to the right in the fourth. In (a) through (c), we highlight all the locations at a particular x in red. This shows the shape of the channel through which the fluid moves. Note the three-limbed channel in (a), which has vanished in (b). The right limb is continuous with the rightmost red arc in (b), and the center of the three-limbed channel is continuous with the upper, hourglass-shaped channel in (b). The hourglass-shaped channel will turn out to be the main channel for fluid flow at low frequency, and the rightmost arc will become important at high frequency. In (c), the upper channel has connected into a larger network again, while the righthand channel has split into two regions. In (d), we show just the pore space itself, in the orientation which will be used in all subsequent figures, with the x axis extending to the right.

(a) Frequency = 28kHz

(b) Frequency = 282kHz

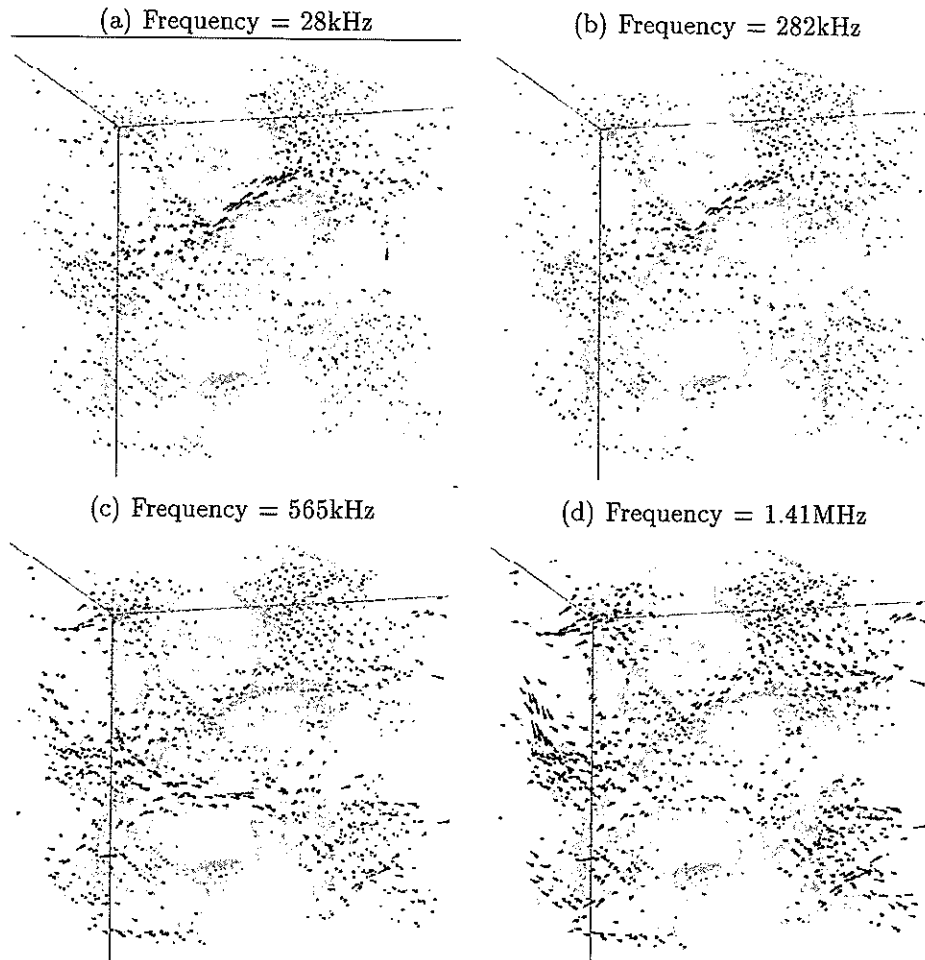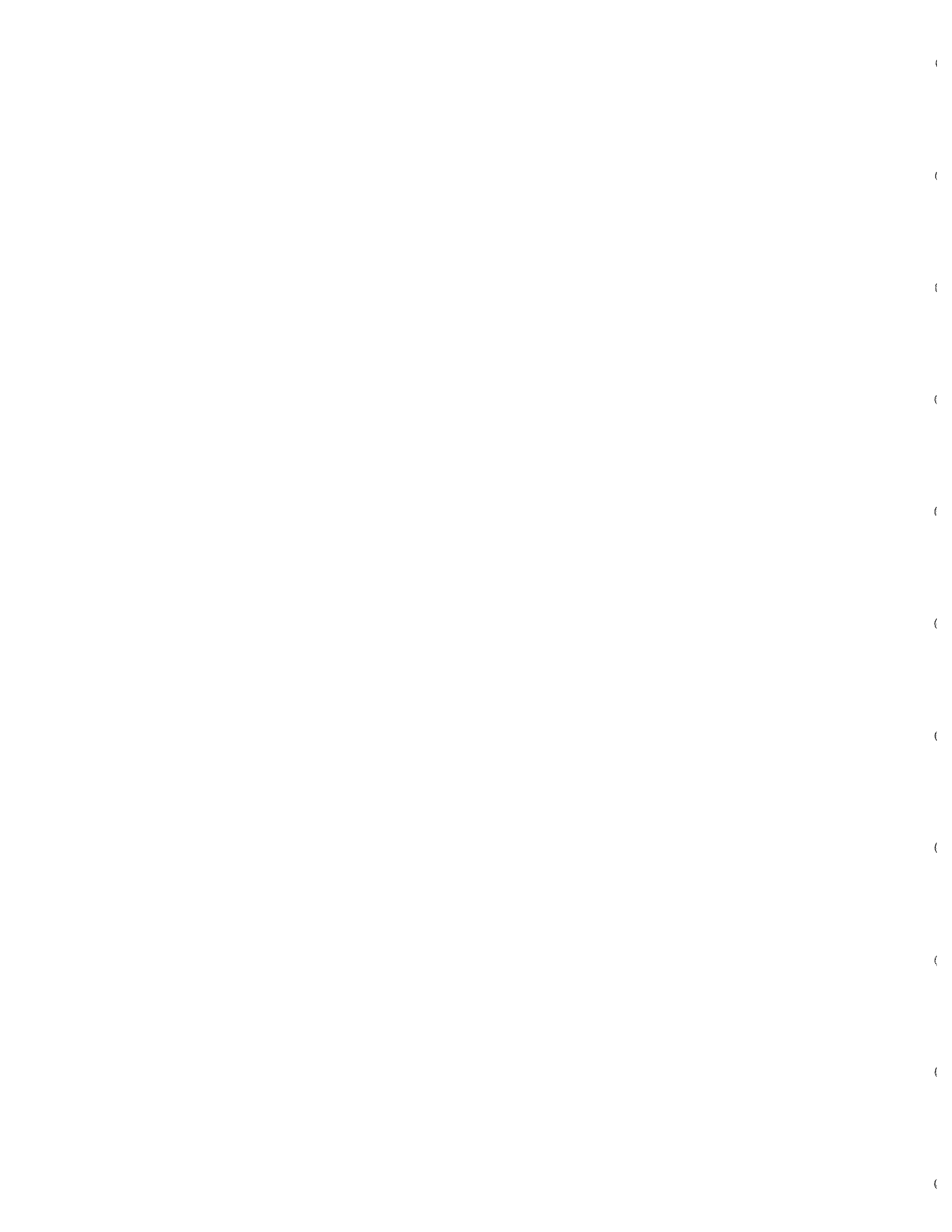(c) Frequency = 565kHz

(d) Frequency = 1.41MHz

Figure 2: Velocity fields at different driving frequencies. We show only a subset of the simulations because figures at other frequencies look similar to the top two cases. The scale of the velocity vectors is not the same. The scale in (b) is four times that in (a); in (c), ten times that in (a); and in (d), 20 times.

(a) Frequency = 28kHz

(b) Frequency = 282kHz

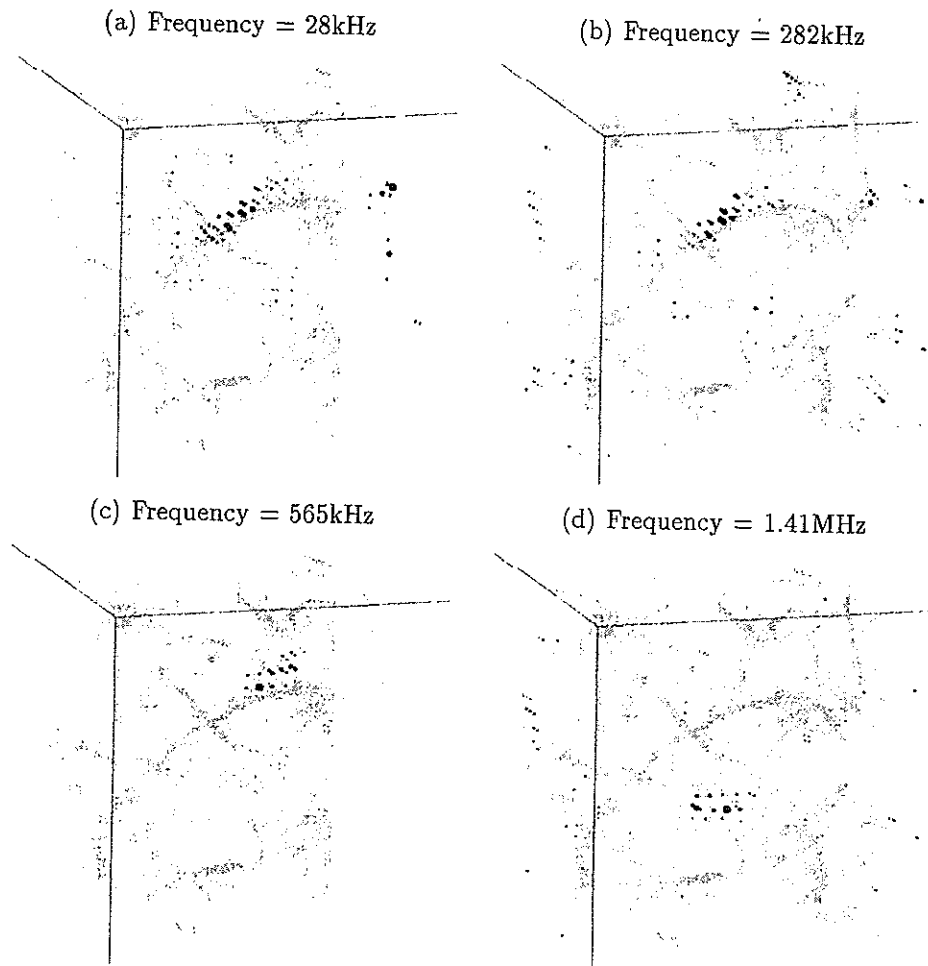(c) Frequency = 565kHz

(d) Frequency = 1.41MHz

Figure 3: Dissipation at different driving frequencies. We show only a subset of the simulations because figures at other frequencies look similar to the first case. The size and darkness of the dots indicate the local rate of viscous dissipation at each location, though the scale is different in each case. See Table 2 for the scales.

6–13

(a) Frequency = 28kHz (b) Frequency = 282kHz

(c) Frequency = 565kHz (d) Frequency = 1.41MHz

Advanced   Delayed

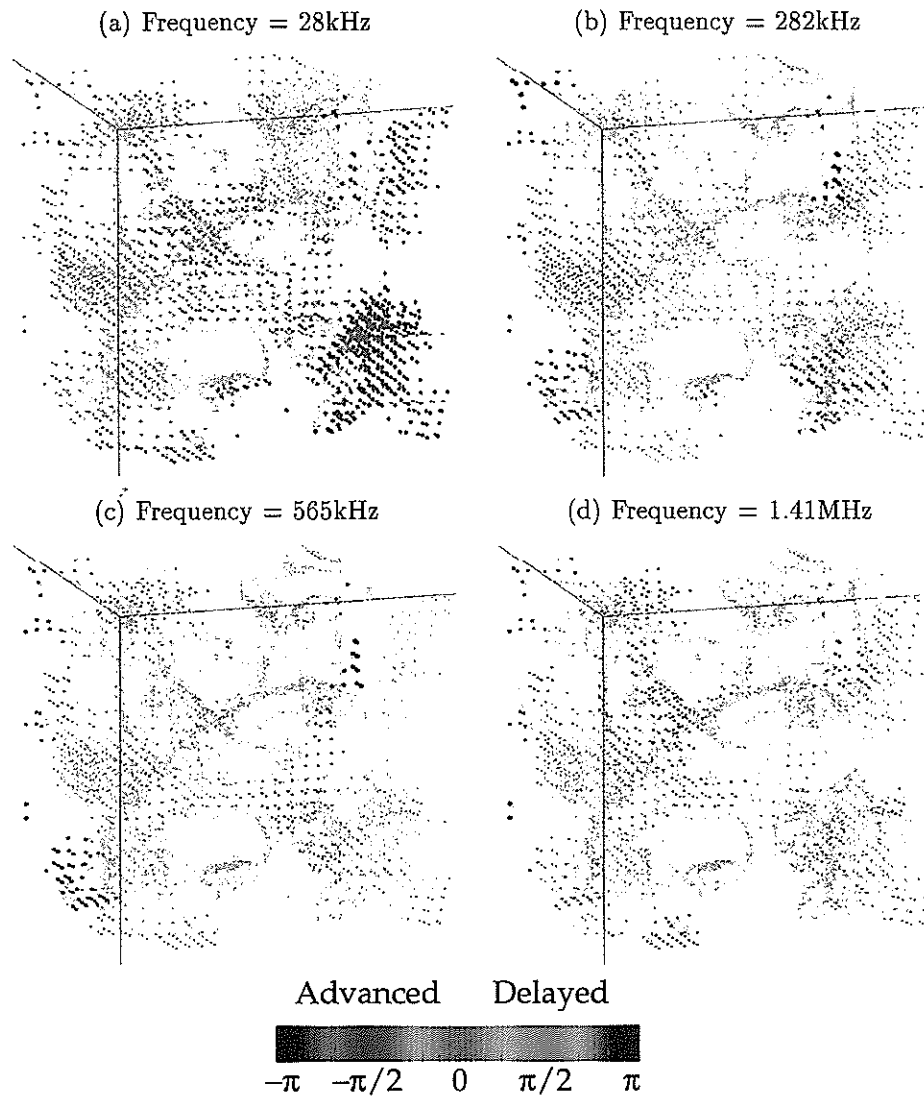$-\pi$ $-\pi/2$ 0 $\pi/2$ π

Figure 4: Pressure at different driving frequencies. We show only a subset of the simulations because figures at other frequencies look similar to the first case. The size of the dots indicates the amplitude of pressure variation at each location, and the color indicates phase as shown. The maximum amplitudes in MPa are (a), 17; (b), 4.1; (c), 2.4; and (d), 0.97.